Simulations of a Conducting Sphere Moving through Magnetized Plasma: Alfvén Wings, Slow Magnetosonic Wings, and Drag Force

Nicholas J. Corso 1 and Dong Lai 12,1

¹Department of Astronomy, Center for Astrophysics and Planetary Science, Cornell University, Ithaca, NY 14853, USA

²Tsung-Dao Lee Institute, Shanghai Jiao-Tong University, Shanghai, China

ABSTRACT

Plasma-mediated interaction between astrophysical objects can play an important role and produce electromagnetic radiation in various binary systems, ranging from planet-moon and star-planet systems to binary compact objects. We perform 3D magnetohydrodynamic numerical simulations to study an ideal magnetized plasma flowing past an unmagnetized conducting sphere. Such flow generates magnetic disturbances and produces a drag force on the sphere, and we explore the corresponding drag coefficient as a function of the flow speed relative to Alfvén speed and the β parameter of the background plasma. We find that the drag is generally well-described by the Alfvén wing model, but we also show that slow magnetosonic waves provide a correction through their own wing-like features. These give rise to a nontrivial dependence of the drag coefficient on the plasma β , as well as enhanced drag as the flow speed approaches the Alfvén speed.

1. INTRODUCTION

Viscous drag on a sphere moving through a fluid is a classic problem in hydrodynamics, from its analytical conception in Stokes's law (Stokes 1851), through advances to higher Reynolds number using experimental and computational techniques (see Tiwari et al. 2020 for a comprehensive review). The problem is best summarized through the relationship between the drag coefficient and Reynolds number, which reveals changes in scalings as the flow transitions from laminar to vortex formation and shedding to turbulence. Despite the idealized setup of this problem, it has found a wide array of applications in the physical sciences. What happens if the fluid is replaced by a magnetized plasma and the sphere is conducting? Is there a similar construction that we may use to describe this type of flow?

This problem is relevant for a number of astrophysical scenarios where highly magnetized objects interact with weakly or unmagnetized bodies. In particular, magnetic interaction may play an important role and lead to electromagnetic radiation in various types of binaries, including planet-moon systems (Goldreich & Lynden-Bell 1969; Neubauer 1990; Bagenal & Dols 2020), star-planet systems (Li et al. 1998; Preusse, S. et al. 2006; Laine & Lin 2011; Lai 2012; Saur 2018; Strugarek 2023; Lee & Owen 2025), and binary compact objects (Hansen &

Email: njc86@cornell.edu, dl57@cornell.edu

Lyutikov 2001; Wu et al. 2002; Dall'Osso, S. et al. 2006; Lai 2012; Wang et al. 2016; Most & Philippov 2022, 2023; Ressler et al. 2024; Mahlmann & Beloborodov 2025). In most cases, the strength of the radiation and its detectability are highly uncertain. While there are appreciable qualitative differences across the systems listed above, there are unifying themes which are useful to consider generally. For instance, the development of a magnetic flux tube connecting the objects and its subsequent stressing and flaring are discussed in the context of planet-moon interactions (Goldreich & Lynden-Bell 1969), star-planet interactions (Lanza 2013) and binary compact object interactions (Lai 2012; Most & Philippov 2022).

The concept of this connecting flux tube can be traced back to the construction of Drell et al. (1965), who considered the model of an ideal conductor (treated as a rectangular bar) moving with velocity $\mathbf{v_0}$ in a lossless plasma with a uniform magnetic field B_0 , to emulate a satellite traveling through Earth's magnetic field. Their analysis is two-dimensional (i.e. the body is infinite in extent in the direction perpendicular to $\mathbf{v_0}$ and $\mathbf{B_0}$), and assumes that the conductor has the same internal magnetic field as the external field. In the linear regime, when the magnetic perturbation $|\delta \mathbf{B}| \sim (v_0/v_A) B_0$ (where v_A is the Alfvén speed) is much less than B_0 , they concluded that the magnetic disturbances of the plasma would propagate as Alfvén waves dragged by the background flow to produce wakes that they named "Alfvén wings." The power radiated through the Alfvén

wings drags the conductor. Neubauer (1980) extended this picture into the regime of $v_0 \lesssim v_A$ in applying the Alfvén wing picture to the system of Jupiter and Io, and included resistive effects. The author claimed that the Alfvén wings form an effective conductance which helps to close the circuit around Io. In particular, under highly magnetized conditions, the Alfvén wave along the wing can bounce off Jupiter and return to Io before the moon has moved away, a closed current system can connect the two bodies, reminiscent of the unipolar inductor model proposed by Piddington (1967) and Goldreich & Lynden-Bell (1969). In general astrophysical binary systems, stellar winds may overwhelm the Alfvén wings, preventing the latter from connecting the objects and instead directing them out to infinity, a case referred to as a pure Alfvén wing (Neubauer 1998). In recent years, magnetic interactions between stars (including stellar winds) and exoplanets have been studied using numerical simulations (e.g. Strugarek et al. 2014, 2015; De Colle et al. 2025), but a general understanding of how a conducting body interacts with an external magnetized plasma and how the drag force and dissipation depend on the plasma properties, the velocity, and the internal magnetic field of the body, is lacking.

In this paper, we begin a series study of the interaction between a moving conductor and an ideal magnetized plasma. We employ three dimensional magnetohydrodynamic (MHD) simulations to find steady-state solutions for the flow and develop a framework for characterizing the drag coefficient as a function of the body's velocity and internal magnetic field and the properties of the magnetic plasma. This paper examines the zero internal field cases; future papers will consider more general magnetic configurations. This paper is organized as follows: in Section 2, we introduce the numerical methods for our simulations and the problem setup; in Section 3, we present the results of a fiducial simulation to develop the qualitative picture of the interaction, and we show the observed scaling with the canonical parameters of the problem; we summarize these results in Section 4.

2. PROBLEM SETUP AND METHOD

We consider a conducting sphere of radius R moving with velocity $\mathbf{v_0} = -v_0 \hat{\mathbf{z}}$ in a magnetized plasma. Far from the sphere $(r \gg R)$, the plasma density is ρ_0 , and the magnetic field is $\mathbf{B} = B_0 \hat{\mathbf{x}}$. In the rest frame of the conductor, the flow velocity is $\mathbf{v} = v_0 \hat{\mathbf{z}}$ at $r \gg R$ (see Figure 1).

To simulate our system we use PLUTO (Mignone et al. 2007), a MHD code designed with a modular structure to handle a variety of astrophysical contexts. In our case, we evolve the idealized MHD equations in flux-

conservative form,

$$\frac{\partial \rho}{\partial t} + \nabla \cdot (\rho \mathbf{v}) = 0, \quad (1)$$

$$\frac{\partial \mathbf{m}}{\partial t} + \nabla \cdot \left(\mathbf{m} \mathbf{v} - \frac{\delta \mathbf{B} \mathbf{B}}{4\pi} - \frac{\mathbf{B}_{bkg} \delta \mathbf{B}}{4\pi} \right) + \nabla p_t = 0, \quad (2)$$

$$\frac{\partial E_t}{\partial t} + \nabla \cdot \left[(E_t + p_t) \mathbf{v} - \frac{(\mathbf{v} \cdot \delta \mathbf{B}) \mathbf{B}}{4\pi} \right] = 0, \quad (3)$$

$$\frac{\partial (\delta \mathbf{B})}{\partial t} - \nabla \times (\mathbf{v} \times \mathbf{B}) = 0, \quad (4)$$

where ρ is the plasma mass density, \mathbf{v} is the velocity, $\mathbf{m} = \rho \mathbf{v}$ is the momentum density, p is the gas pressure, and

$$\mathbf{B}(\mathbf{r},t) = \mathbf{B}_{bkg}(\mathbf{r}) + \delta \mathbf{B}(\mathbf{r},t). \tag{5}$$

Here, $\mathbf{B}_{bkg}(\mathbf{r})$ is a fixed background magnetic field (see below), and $\delta \mathbf{B}$ (which is not necessarily small) is an evolved difference from the background field. The following are defined to represent the evolved terms for the total pressure and energy density,

$$p_t = p + \frac{\delta \mathbf{B}^2}{8\pi} + \frac{\delta \mathbf{B} \cdot \mathbf{B}_{\text{bkg}}}{4\pi},\tag{6}$$

$$E_t = \rho \varepsilon + \frac{1}{2} \left(\rho \mathbf{v}^2 + \frac{\delta \mathbf{B}^2}{4\pi} \right), \tag{7}$$

where ε is the plasma internal energy per unit mass. We note that PLUT0 itself adopts a convention in which the factor of $1/\sqrt{4\pi}$ is absorbed into the definition of the magnetic field, but for this paper we will instead choose the CGS convention. These equations are closed by an ideal equation of state,

$$\rho \varepsilon = \frac{p}{\gamma - 1},\tag{8}$$

where we choose $\gamma = 5/3$, the adiabatic index of a monoatomic ideal gas.

With this setup, the key dimensionless parameters of our system are the Alfvén Mach number and the plasma β , defined by

$$M_{\rm A} \equiv \frac{v_0}{v_{\rm A,0}}, \quad \beta \equiv \frac{p_0}{B_0^2/4\pi} = \frac{c_{\rm s,0}^2/\gamma}{v_{\rm A,0}^2},$$
 (9)

where $v_{\rm A,0} = B_0/\sqrt{4\pi\rho_0}$ and $c_{\rm s,0} = \sqrt{\gamma p_0/\rho_0}$ are the Alfvén and sound speeds of the background flow (associated with ρ_0 , p_0 , and B_0).

For all simulations, we use the second-order finite volume method that evolves all quantities according to their cell-centered values. We employ a third order weighted essentially non-oscillatory (WENO3) scheme for reconstruction (Yamaleev & Carpenter 2009) from cell centers to cell faces. For most cases, we employ the

linearized Roe Riemann solver for computing fluxes at the cell faces (Roe 1981), but in some cases with high flow speeds and low plasma β , we must rely on the more diffusive Harten-Lax-van Leer Discontinuities (HLLD) Riemann solver (Harten et al. 1983; Miyoshi & Kusano 2005). We use hyperbolic divergence cleaning to enforce the $\nabla \cdot \mathbf{B}$ condition during evolution (Dedner et al. 2002; Mignone & Tzeferacos 2010; Mignone et al. 2010).

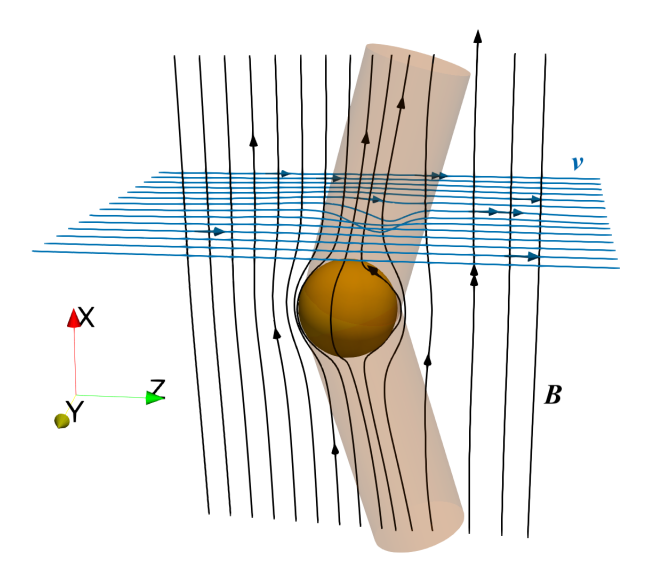


Figure 1. A sketch of the simulated system while it is in a steady state. The black lines are the magnetic field lines in the x-z plane, which asymptotically approach $\mathbf{B}=B_0\hat{\mathbf{x}}$ for $r\gg R$, where R is the radius of the conducting sphere. The blue lines are the velocity field lines in the x=2R plane, which similarly approach an asymptotic value of $\mathbf{v}=v_0\hat{\mathbf{z}}$ for $r\gg R$. The orange sphere in the center represents the conductor, and the transparent orange cylinders emerging from it represent the theoretical locations of the Alfvén wing characteristics.

2.1. Computational Domain and Boundary Conditions

All simulations are run on a discretized grid using spherical coordinates (r, θ, ϕ) , with a hard spherical conductor surface placed as the inner boundary and the outer boundary $r_{\text{out}} \gg R$ set to have a zero-gradient outflow condition. Unless stated otherwise, the simulation domain spans $r \in [R, 10R]$ and the full unit sphere, using $N_r \times N_\theta \times N_\phi = 100 \times 64 \times 128$ grid points, where the radial points are spaced logarithmically and the angular points uniformly. The polar axis coordinate singularity is avoided due to the fact that cell-centered quantities are evolved, but compression of cells near this boundary still prohibitively limits the simulation speed due to the Courant–Friedrichs–Lewy (CFL) condition.

To avoid this problem, we follow PLUTO and employ a "ring-averaging" technique, in which cells close to the polar axis are combined to effectively increase their size, increasing the azimuthal resolution by a factor of 2 for every step away from the polar axis until reaching the full resolution. For our fiducial simulations, the cells adjacent to the polar axis effectively have an azimuthal resolution of $N_{\phi}=16$. The boundary condition at the polar axis is set such that cells receive information from across the pole, and the azimuthal boundary condition is periodic.

Each simulation is initialized in the computational domain with a plasma of mass density ρ_0 and pressure p_0 traveling with the velocity of a potential flow,

$$\mathbf{v} = v_0 \cos \theta \left[1 - \left(\frac{R}{r} \right)^3 \right] \hat{\mathbf{r}} + v_0 \sin \theta \left[1 + \frac{1}{2} \left(\frac{R}{r} \right)^3 \right] \hat{\theta}.$$
(10)

Note that at r = R this already satisfies the hard boundary of the conductor (i.e. $v_r = 0$), and far from the sphere the velocity approaches $\mathbf{v} = v_0 \hat{\mathbf{z}}$. We assume that the conductor has no interior magnetic field $\mathbf{B}_{\text{in}} = 0$. The magnetic field in the computational domain is initialized such that it maintains continuity in B_r across the conductor boundary and asymptotically approaches $\mathbf{B_0} = B_0 \hat{\mathbf{x}}$ at $r \gg R$. The combination of these two conditions specifies the fixed "background" field \mathbf{B}_{bkg} introduced in Equation (5),

$$\mathbf{B}_{\text{bkg}} = B_0 \hat{\mathbf{x}} - \left(\frac{R}{r}\right)^3 \frac{B_0}{2} \left[3(\hat{\mathbf{r}} \cdot \hat{\mathbf{x}})\hat{\mathbf{r}} - \hat{\mathbf{x}}\right]. \tag{11}$$

The asymptotic behavior of \mathbf{v} and \mathbf{B}_{bkg} can be seen in Figure 1, which provides a schematic of the steady-state Alfvén wing behavior. Our simulations start with the initial $\delta \mathbf{B} = \mathbf{B} - \mathbf{B}_{bkg} = 0$.

Since the described initial conditions represent a background flow passing the conductor, it is vital that this flow is preserved at large distances from it. On its own, the zero-gradient outflow condition at $r_{\text{out}} = 10R$ could result in divergent behavior since perturbations may provide feedback to the background flow. As such, following the procedure of Laune et al. (2024), we introduce a damping zone in the region 8R < r < 10R. In this region, for a given evolved variable in conservative form, A, which has a background value of A_0 , a damping term is introduced to the right hand side of the MHD equations. This term, denoted D_A , takes the following form,

$$D_A = -\zeta(x)\frac{A - A_0}{T_d},\tag{12}$$

where the tapering function is given by

$$\zeta(x) = \begin{cases} 1 - 6x^2 + 6x^3 & 0 \leqslant x \leqslant \frac{1}{2} \\ 2(1-x)^3 & \frac{1}{2} < x \leqslant 1, \end{cases}$$
 (13)

with

$$x = 1 - \frac{r - 8R}{2R}. (14)$$

We set the damping timescale T_d using the fastest characteristic speed across the damping zone,

$$T_d \simeq \frac{2R}{\max(v_0, v_{\text{fast.0}})},\tag{15}$$

where $v_{\text{fast,0}} = \sqrt{c_{\text{s,0}}^2 + v_{\text{A,0}}^2}$ is the maximum value of the fast magnetosonic wave speed.

2.2. Analysis and Observables

We are interested in measuring the drag force on the conductor. A direct evaluation of this quantity may be obtained by taking a volume integral of the rate of change of momentum density (see Eq. 2),

$$\mathbf{F}_{\text{drag}} = \int \frac{\partial \mathbf{m}}{\partial t} dV$$
$$= -\oint \left(\mathbf{m} \mathbf{v} - \frac{\delta \mathbf{B} \mathbf{B}}{4\pi} - \frac{\mathbf{B}_{\text{bkg}} \delta \mathbf{B}}{4\pi} + p_t \mathbf{I} \right) \cdot d\mathbf{A}. \quad (16)$$

To evaluate Eq. (16), we choose our surface to be a sphere that encloses the conductor. We evaluate this drag force in terms of the mechanical power imparted onto the conductor, i.e., $\dot{E} = \mathbf{F}_{\text{drag}} \cdot \mathbf{v_0} = F_{\text{drag},\mathbf{z}}v_0$. Note that we adopt the convention that $\dot{E} > 0$ corresponds to a drag that slows down the object in the plasma rest frame. Evaluating Eq. (16) at radius r, we find

$$\dot{E}(r) = -r^2 v_0 \oint \left(m_z v_r - \frac{\delta B_z B_r}{4\pi} - \frac{B_{\text{bkg},z} \delta B_r}{4\pi} + p_t \cos \theta \right) d\Omega. \quad (17)$$

The Alfvén wing model (Drell et al. 1965) suggests that the power imparted onto the conductor should derive from the perturbed Poynting flux propagating along the Alfvén wings. For $v_0 \lesssim v_{\rm A,0}$, the Alfvén wave amplitude at $r \sim R$ is of order $B_0 v_0 / v_{\rm A}$, and the wing has an area $\sim \pi R^2$. Thus the power is

$$\dot{E} \sim \frac{1}{4\pi} \left(B_0 \frac{v_0}{v_{A,0}} \right)^2 v_{A,0} \left(2\pi R^2 \right)
= \frac{1}{2} B_0^2 R^2 \frac{v_0^2}{v_{A,0}} = 2\rho_0 \pi R^2 v_0^2 v_{A,0}. \quad (18)$$

Motivated by Eq. (18), we define a dimensionless drag coefficient C_A , such that

$$\dot{E} = C_{\rm A} \rho_0 R^2 v_0^2 v_{\rm A,0},\tag{19}$$

with $C_{\rm A}=C_{\rm A}(M_{\rm A},\beta)$ depending only on $M_{\rm A}$ and β (see Eq. 9).

In our study, we run a given simulation until $C_{\rm A}$ reaches a constant value, indicating that the simulation has reached a steady state. This usually takes several crossing times, $t_{cross} = R/v_0$, to achieve but may occur more rapidly. For this study, we run simulations for $M_A \in [0.003, 1]$ spaced logarithmically, and for $\beta = 200, 2, \text{ and } 0.02.$ We also perform additional runs for $M_{\rm A}=0.01,0.1$ and $\beta\in[0.002,200]$ spaced logarithmically to focus on the scaling of C_A with β in the linear regime. Since some of these cases approach supersonic speeds, we switch to the HLLD Riemann solver when $M_{\rm A} \geq 0.1$ for $\beta = 0.02$ and when $M_{\rm A} \geq 0.7$ for $\beta = 2$ to improve the robustness of the simulations. Note that when $\beta = 0.02$ and $M_A \geq 0.7$, the simulations fail due to the development of a strong evacuated region in front of the conductor, leading to failures in our numerical method.

3. RESULTS

3.1. Fiducial Run

Our fiducial run has $M_{\rm A}=v_0/v_{\rm A,0}=0.3$ and $\beta=2$. In Figs. 2 and 3, we depict several diagnostic variables after a steady state has been achieved. The evolved quantities ($\delta {\bf B}$ and ${\bf v}$) show noticeable perturbations along the Alfvén wing characteristics, which are defined as

$$\mathbf{c}_{\mathbf{A}}^{\pm} = \mathbf{v} \pm \mathbf{v}_{\mathbf{A}},\tag{20}$$

where $\mathbf{v}_{\rm A} \equiv \mathbf{B}/\sqrt{4\pi\rho}$. On the front side of the wing, we observe an enhancement of the magnetic field and a reduction in the gas density and pressure. Directly along $\mathbf{c}_{\rm A}^\pm$, we observe a narrow region that has nearly zero velocity. This region co-moves with the conductor, and the enhanced magnetic flux is frozen in, creating a narrow obstacle that the background plasma passes around. This behavior is highlighted in Figure 4, which shows some of the diagnostics in the x=-2R plane. The flow drags the magnetic field lines to form loops around the Alfvén wing.

Figures 2–4 also reveal some features not directly associated with the Alfvén wings. For instance, immediately downstream of the conductor is a small bubble which exhibits enhanced magnetic field strength, density, and pressure. This region is partially trapped, confined by magnetic field lines wrapping around the conductor. We do observe a density enhancement downstream of this

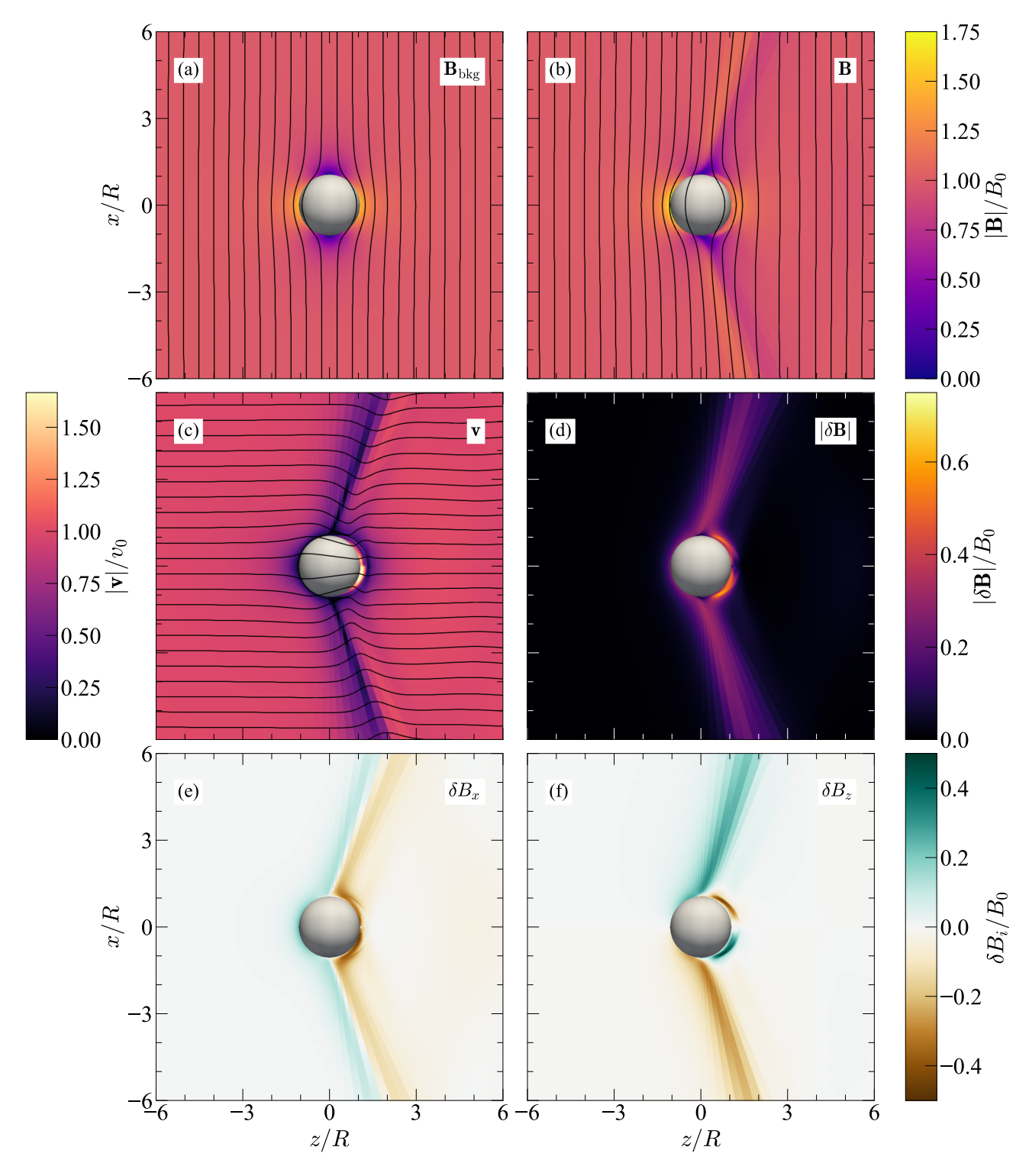


Figure 2. Diagnostic parameters for our fiducial run, with $M_{\rm A}=0.3$, $\beta=2$, on the x-z plane after the simulation has achieved a steady state. The conductor is shown as a gray sphere in the center of the domain. Vector quantities are plotted with field lines placed in front of a background which displays magnitude. The field lines initialize at y=0.15 when r=10R and may vary in y across the domain. From left-to-right, top-to-bottom, the quantities are (a) $\mathbf{B}_{\rm bkg}$, (b) \mathbf{B} , (c) \mathbf{v} , (d) $|\delta\mathbf{B}|$, (e) δB_x , and (f) δB_z . All evolved quantities show disturbances along the Alfvén wing characteristics. We note that the velocity field lines wrap around the wings since motion stops entirely along the characteristics.

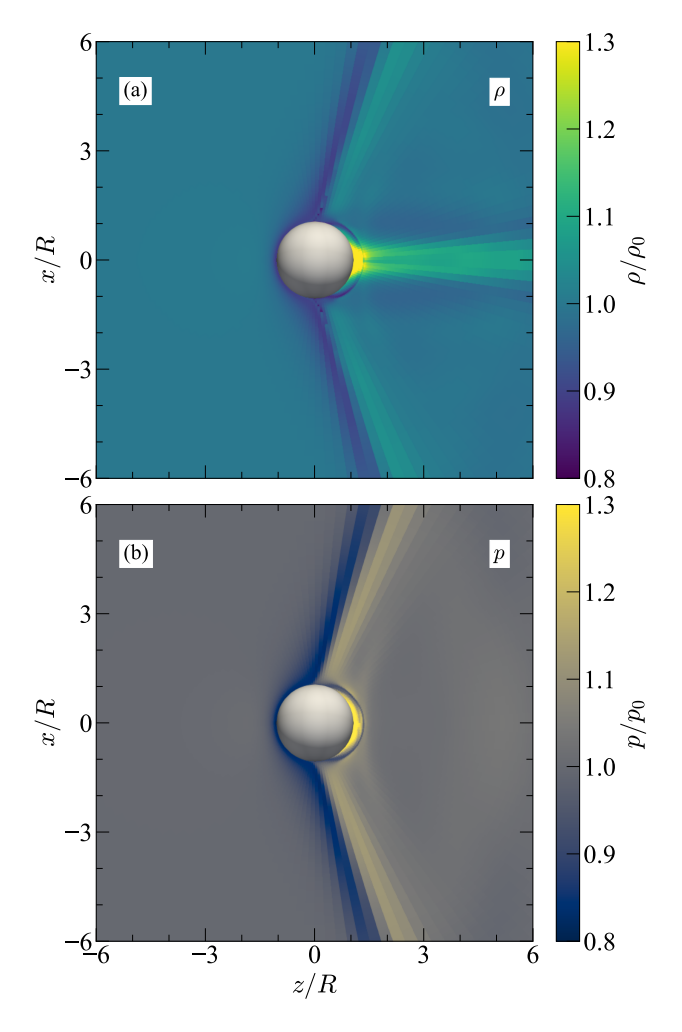


Figure 3. Density (a) and pressure (b) for our fiducial run, with $M_{\rm A}=0.3,~\beta=2,$ on the x-z plane after the simulation has achieved a steady state.

feature, but it is transported by the background flow, so in the cases of low $M_{\rm A}$, it carries significantly less energy away from the conductor compared to the Alfvén wings.

Figure 5 depicts the drag coefficient $C_{\rm A}$ (see Eq. 19) as a function of time for our fiducial run. After an initial transient phase, we find that the simulation rapidly arrives at a steady state, where evaluations of $C_{\rm A}$ at different radii achieve the same value. We use this level of agreement as a diagnostic for the quality of the simulation, and runs that do not converge to a single value of $C_{\rm A}$ over time are rerun at higher resolution.

3.2. M_A - and β -Dependence

Figure 6 depicts $C_{\rm A}$ as a function of $M_{\rm A}$ at our fiducial $\beta=2$. For low values of $M_{\rm A}$, the drag coefficient remains roughly constant, at a value $C_{\rm A}\approx 1.2$, indicating a strong agreement with the Alfvén wing model in

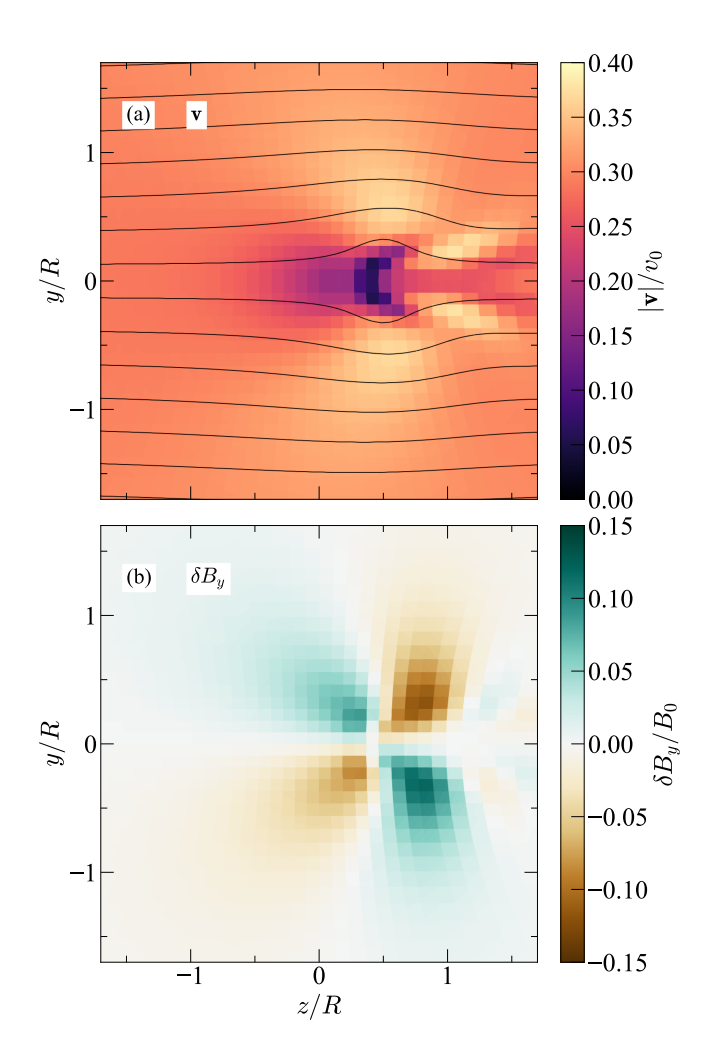


Figure 4. Diagnostic parameters for our fiducial run on the x = -2R plane (seen from below) after the simulation has achieved a steady state. Shown are (a) \mathbf{v} and (b) δB_y . The vector field lines for \mathbf{v} initialize at x = 2.5R since there is a strong out-of-plane component close to the wing [see Figure 2(c)].

this regime. However, for $M_{\rm A} \gtrsim 0.1$, we find a noticeable increase in $C_{\rm A}$. In this case, the system enters a nonlinear regime, where the wings point so far forward that they disturb the flow downstream of the conductor.

Figure 7 shows the $C_{\rm A}$ vs. $M_{\rm A}$ relations for different values of β . For each case, we see the same general pattern, where sub-Alfvénic flows exhibit a constant value of $C_{\rm A}$, in good agreement with the standard Alfvén wing picture, but flows with larger $M_{\rm A}$ exhibit a noticeable increase in the drag coefficient. For the $\beta=0.02$ case, we find that this transition to a higher drag sets in at lower values of $M_{\rm A}$. Indeed, the upward swing of $C_{\rm A}$ occurs when $v_0 \approx c_{\rm s,0}$. Additionally, even in the sub-

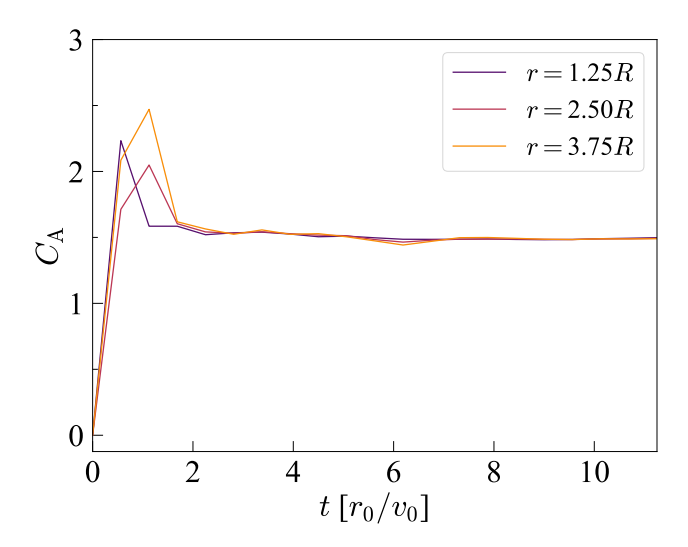


Figure 5. Time evolution of the drag coefficient $C_{\rm A}$ (see Eq. 19) measured at different radii (see Eq. 17) in our fiducial run ($M_{\rm A}=0.3$ and $\beta=2$). For all simulations, the system is evolved until the value for $C_{\rm A}$ stabilizes, as shown in this case. $C_{\rm A}$ is evaluated at $r=\{1.25,2.50,3.75\}R$ (purple, magenta, and orange, respectively).

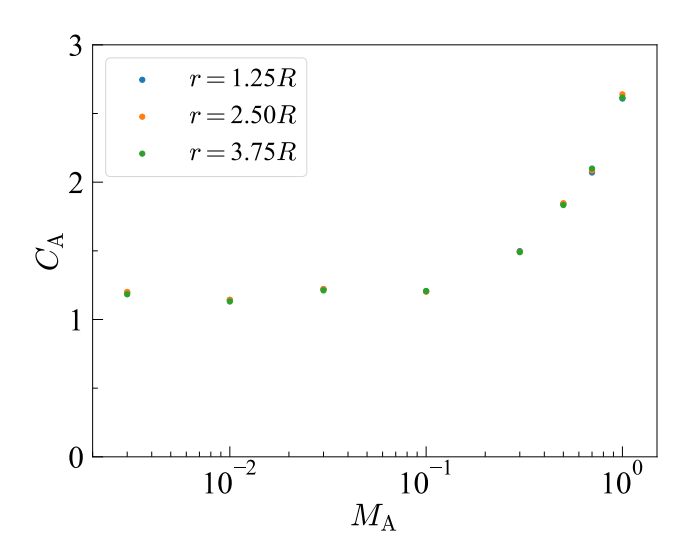


Figure 6. The drag coefficient $C_{\rm A}$ measured at different radii as a function of $M_{\rm A}$ for $\beta=2$. The values are obtained following the procedure outlined in Figure 5. The residual spread among different radii is interpreted as a level of "error" in our measurement. The value of $C_{\rm A}$ is roughly constant for sub-Alfvénic speeds, but noticeably increases as $M_{\rm A}$ approaches unity.

Alfvénic regime where the Alfvén wing model appears robust, we find that C_A strictly increases with β .

Figure 8 focuses on this sub-Alfvénic regime by plotting $C_{\rm A}$ as a function of β for $M_{\rm A}=0.01$ and $M_{\rm A}=$

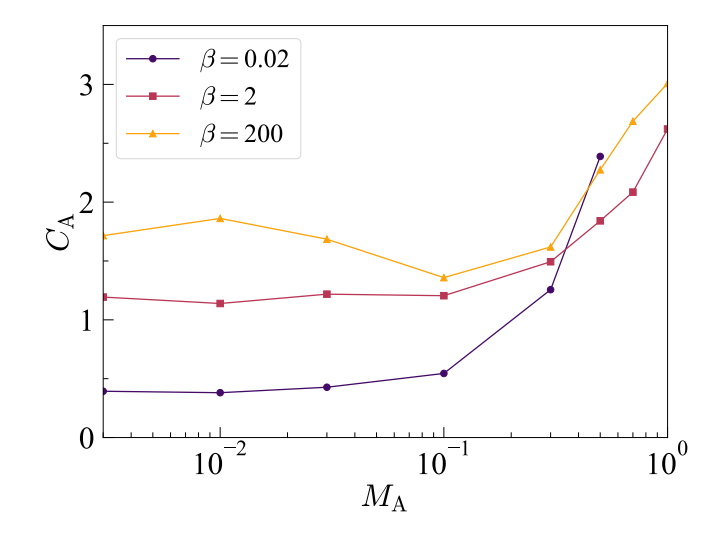


Figure 7. The drag coefficient C_A measured at r = 1.25R as a function of M_A for $\beta = 0.02, 2, 200$ (purple circle, magenta square, yellow triangle).

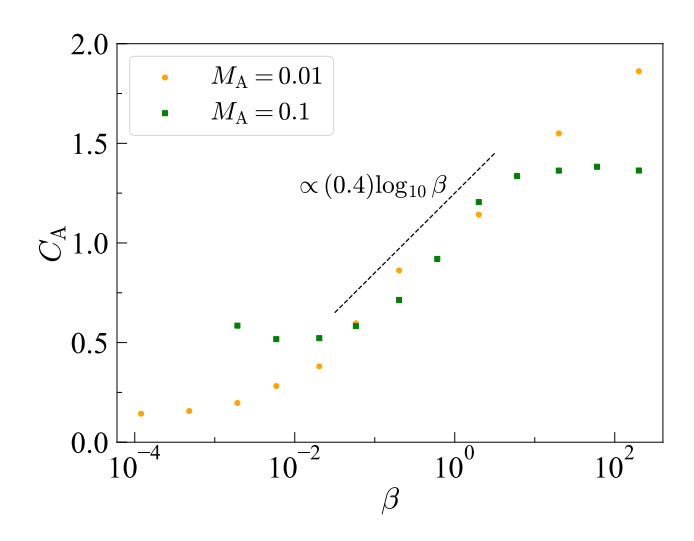


Figure 8. The drag coefficient $C_{\rm A}$ as a function of β , for $M_{\rm A}=0.01$ (yellow circle) and $M_{\rm A}=0.1$ (green square). The black dashed line indicates the scaling that occurs in the regime where $C_{\rm A}$ is increasing.

0.1. For low values of β , there is no strong relationship between $C_{\rm A}$ and β , but after a transition point, we find that the $C_{\rm A}$ - β relation is well described by $C_{\rm A} \simeq (0.4) \log_{10} \beta$. The transition point where this scaling begins varies between the two cases but corresponds to the point where the condition $M_{\rm A} \simeq c_{\rm s}/v_{\rm A}$ holds. We note that the $M_{\rm A}=0.1$ case shows a high β regime where this trend again flattens off, but that this is absent in the $M_{\rm A}=0.01$ case.

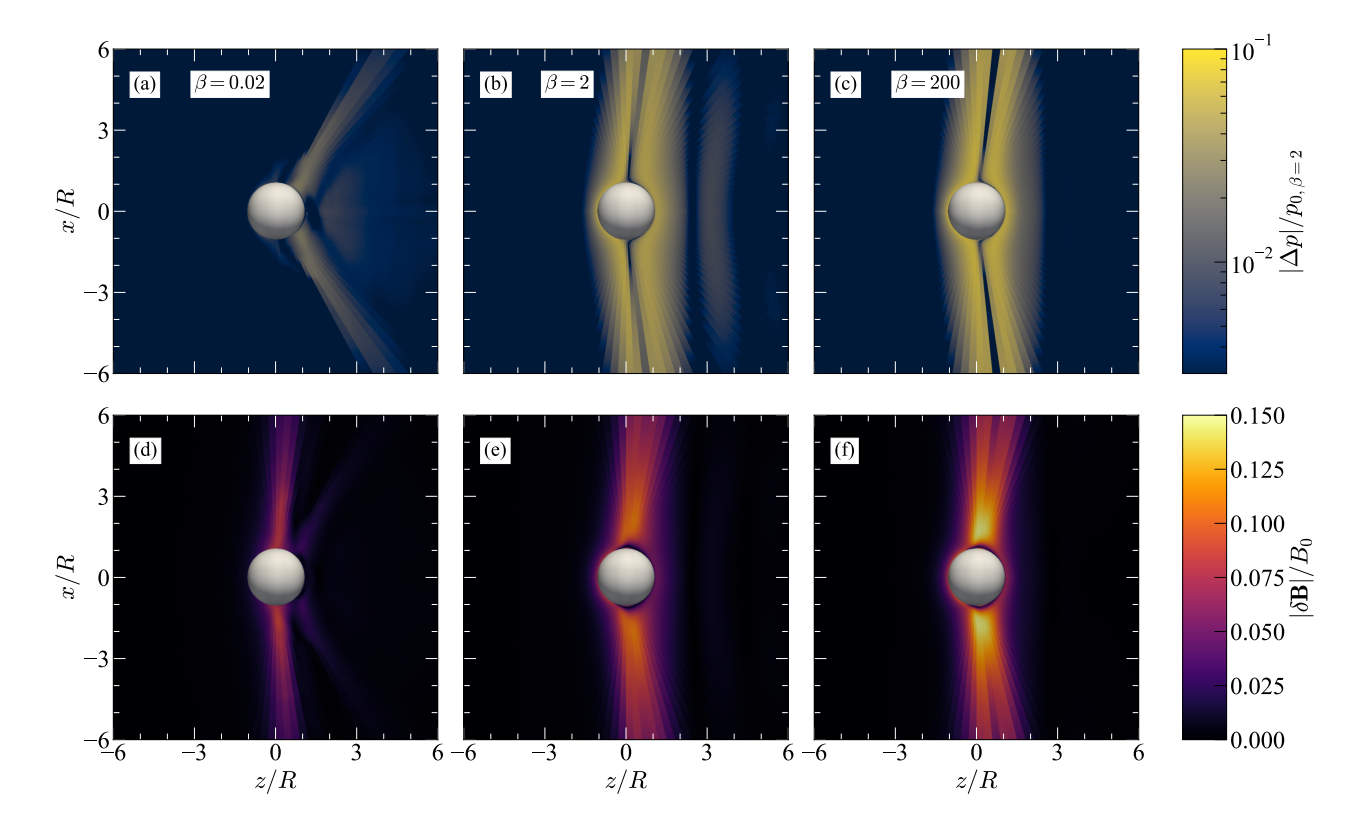


Figure 9. Gas pressure and magnetic field disturbances for $M_{\Lambda} = 0.1$, with different values of β on the x-z plane after each simulation has achieved a steady state. The top row shows $|\Delta p| = |p - p_0|$, normalized by the background pressure of the $\beta = 2$ case, and the bottom row shows $|\delta \mathbf{B}|$.

To explore this trend with β further, we show the disturbances in both the gas pressure and the magnetic field in Figure 9 for several runs with different values of β , all with $M_{\rm A}=0.1$. We see that for the $\beta=0.02$ case, the magnetic disturbance and pressure disturbance have very different patterns. While the former still follows the Alfvén characteristic (Eq. 20), the latter follows a more "inclined" trajectory, corresponding approximately to the characteristic

$$\mathbf{c}_{-}^{\pm} = \mathbf{v} \pm c_{\mathrm{s}} \hat{\mathbf{x}},\tag{21}$$

where $c_{\rm s}=(\gamma p/\rho)^{1/2}$ is the gas sound speed. The "high inclination" of the pressure disturbance for the low β case suggests that it is generated by the slow magnetosonic wave, which is described by the dispersion relation,

$$\left(\frac{\omega}{k}\right)^2 = \frac{1}{2} \left(v_{\rm A}^2 + c_{\rm s}^2 - \sqrt{\left(v_{\rm A}^2 + c_{\rm s}^2\right)^2 - 4v_{\rm A}^2 c_{\rm s}^2 \cos^2\alpha}\right),\tag{22}$$

where α is the angle between the wavevector **k** and the magnetic field, and ω is the angular frequency. Unlike Alfvén waves, which propagate at a group velocity aligned with the magnetic field, the slow waves have

some degree of dispersion, so they have been neglected in the context of magnetic interactions in binary systems since they are believed to be unfocused and unrelated to the Alfvén wing picture (Strugarek 2023; Neubauer 1980). However, in the cases of extreme β , the slow wave group velocity may still effectively collimate in a single direction, approaching $\mathbf{v}_{\text{slow}} \approx c_{\text{s}} \hat{\mathbf{b}}$ in the case of $\beta \ll 1$ and $\mathbf{v}_{\text{slow}} \approx v_{\text{A}} \hat{\mathbf{b}}$ in the case of $\beta \gg 1$, where $\hat{\mathbf{b}}$ is the unit vector aligned with the magnetic field. This suggests that the slow wave could also produce a wing-like structure which is distinct from the Alfvén wing in the former case but collinear in the latter case, which is precisely what occurs in Figure 9.

Figure 10 shows the angular distribution of the contributions to $C_{\rm A}$ for the same three cases depicted in Figure 9:

$$\frac{\partial C_{\mathcal{A}}}{\partial \Omega} = \frac{1}{\rho_0 R^2 v_0^2 v_{\mathcal{A},0}} \frac{\partial E}{\partial \Omega},\tag{23}$$

where we have, from Eq. (17),

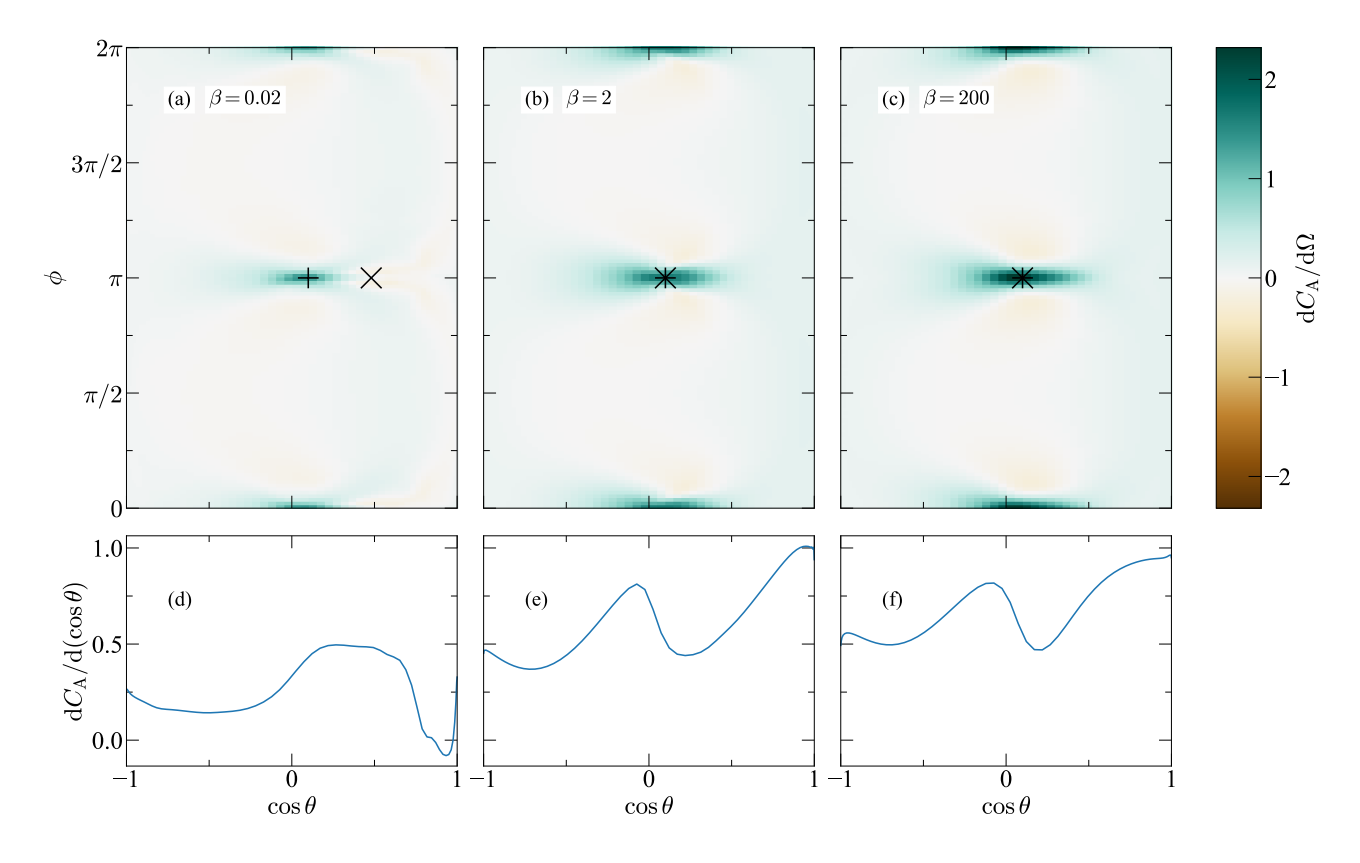


Figure 10. Distribution of the contributions to C_A measured at r = 1.5R over solid angle (top row) and only $\cos \theta$ (bottom row) for $M_A = 0.1$ with different values of β . The contributions from the background flow, defined in Eq. (25), were subtracted out to highlight new features in the steady state. The black plus signs and crosses indicate the locations of the Alfvén and slow wing characteristics, respectively.

$$\frac{\partial C_{A}}{\partial \Omega} = -r^{2} v_{0} \left(m_{z} v_{r} - \frac{\delta B_{z} B_{r}}{4\pi} - \frac{B_{\text{bkg},z} \delta B_{r}}{4\pi} + p_{t} \cos \theta \right).$$
(24)

To highlight interesting features, the contributions from the background flow are subtracted; *i.e.*, since we have $\delta B\big|_{t=0}=0$, we may apply Equation (17) to find the initial drag contribution,

$$\left. \frac{\partial \dot{E}(r)}{\partial \Omega} \right|_{t=0} = -r^2 v_0 \left(\rho_0 v_0^2 + p_0 \cos \theta \right). \tag{25}$$

Due to the symmetry of the initial data, Equation (25) contains a dipolar contribution, which cancels itself out when integrating over the sphere. As such, we lose no important information by subtracting this component out. For what remains we find that much of the energy dissipation is indeed being propagated through the Alfvén wings, but in the case of higher plasma β we see strong contributions at the polar regions as well. This is likely due to the pressure enhancements building up

in front of and behind the sphere. We note that for the $\beta=0.02$ case, the direction of the slow wave points to a collimated region which contributes little to the drag force, and may even hinder it.

Figure 11 shows the same quantities for the case of $M_{\rm A}=0.5$. In this case, the power dissipated by the disturbance is less collimated along the Alfvén characteristics, instead filling the entire region downstream of the conductor. This reflects the nonlinear structure of the wings in the immediate vicinity of the sphere, which modifies the effective size of the obstacle. At larger distances the disturbances would again collimate along the Alfvén characteristics, but the size of the wings reflects the new effective size of the obstacle. This larger disturbance enhances the overall drag imposed on the sphere, resulting in the enhancement seen in Figure 6.

4. SUMMARY AND CONCLUSIONS

We have performed 3D MHD simulations of magnetized flow past an unmagnetized spherical conductor. By numerically calculating the momentum flux car-

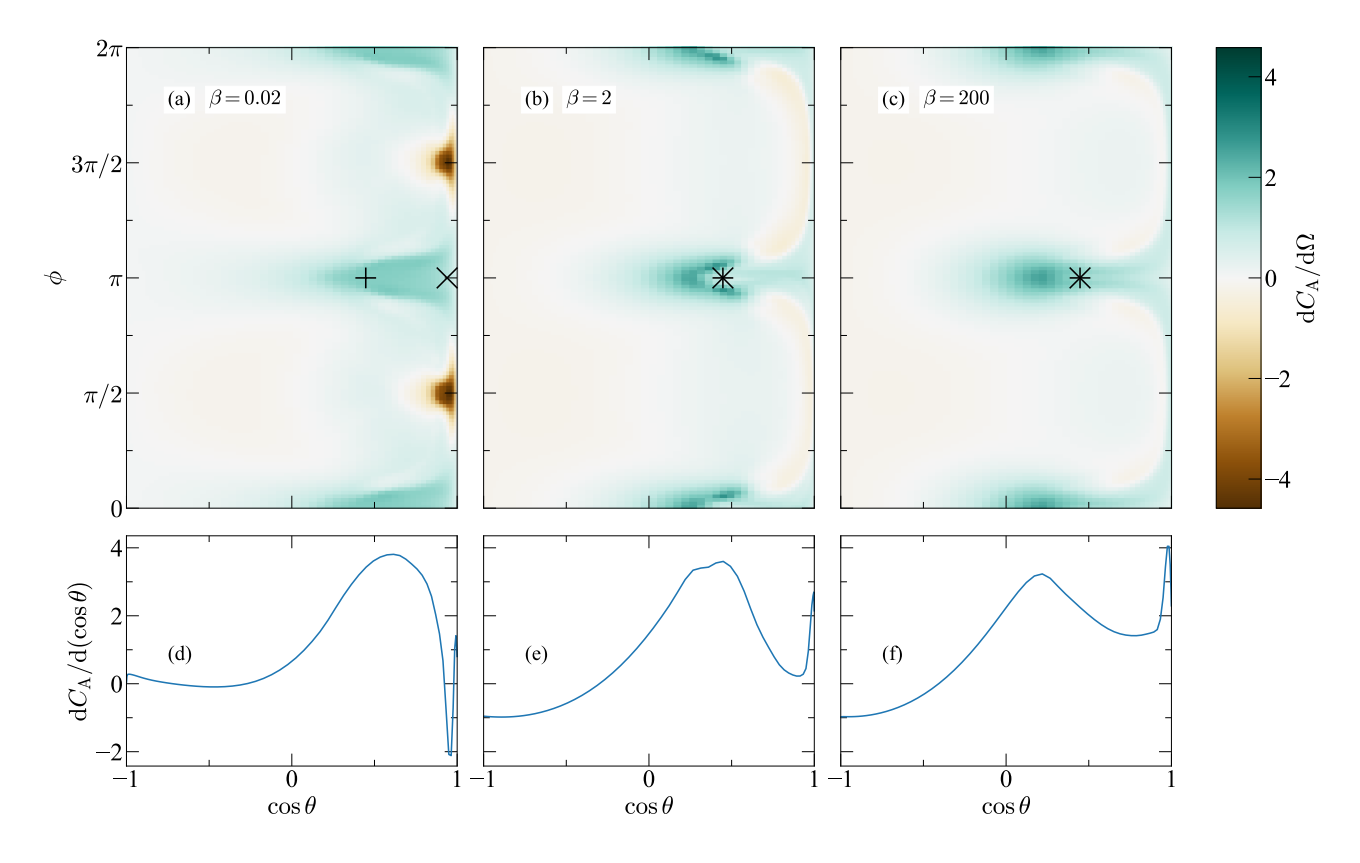


Figure 11. Distribution of contributions to C_A measured at r = 1.5R over solid angle (top row) and only $\cos \theta$ (bottom row) for $M_A = 0.5$ with different values of β . The contributions from the background flow, defined in Eq. (25), were subtracted out to highlight new features in the steady state. The black plus signs and crosses indicate the locations of the Alfvén and slow wing characteristics, respectively.

ried away by the flow and magnetic disturbances along the Alfvén wings, we determine the drag force on the conductor. The drag coefficient $C_{\rm A}$ is a function of two dimensionless parameters, the Alfvén Mach number $M_{\rm A}=v_0/v_{\rm A,0}$, and the plasma $\beta=\left(c_{\rm s,0}^2/\gamma\right)/v_{\rm A,0}^2$. Our simulations reveal distinct Alfvén wing features, and we find consistency with the Alfvén wing model at sub-Alfvénic speeds. Significant deviations occur when $M_{\rm A}$ approaches unity (see Figs. 6–7). We also find a positive correlation between β and $C_{\rm A}$ (see Fig. 8).

The latter result is likely the consequence of a secondary wing associated with the slow magnetosonic wave, which is highly collimated for plasma β far from order unity. When $\beta \ll 1$, the slow magnetosonic wave essentially travels at the speed of sound along magnetic field lines, and when $\beta \gg 1$, it travels at the Alfvén speed. As such, in the low β environments, this 'slow' wing and its corresponding pressure disturbance separates from the Alfvén wing. Meanwhile, the magnetic disturbance remains concentrated along the Alfvén

wing, so it is unclear what sorts of unique observational consequences the slow wing would have. For high β environments, the two wing features are collinear, producing a single enhanced disturbance along the Alfvén wing characteristic.

There are several direct extensions of this work which we intend to pursue. Most compelling are the effects of the internal magnetic field of the conductor, $\mathbf{B}_{\rm in}$. It may give rise to additional magnetic dissipation in the near vicinity of the conductor. There have already been some investigations into this in the context of star-planet (e.g. Strugarek et al. 2014, 2015) and compact object binary (e.g. Most & Philippov 2022, 2023) systems. How the drag force depends on $\mathbf{B_0}$, $\mathbf{B}_{\rm in}$, and other parameters remains unclear.

We also note that our study is currently confined to ideal MHD, so we do not consider the effects of viscosity or resistivity. Viscosity would introduce a boundary layer around the sphere. Resistivity would enable magnetic reconnection, which could dissipate energy from

the Alfvén wings at their boundaries with the surrounding medium. De Colle et al. (2025) include resistivity in their magnetized flow simulations, but it remains an open question how varying the parameter affects the system. Consideration of these features would introduce the Reynolds number and the magnetic Reynolds number as dimensionless canonical parameters of this problem. Indeed, this would bring the system closer to

the original context that inspired this work, viscous flow past a sphere.

ACKNOWLEDGMENTS

This research was partially supported by the NSF grant DGE-2139899.

Software: Matplotlib (Hunter 2007), NumPy (Harris et al. 2020), ParaView (Ayachit 2015).

REFERENCES

Ayachit, U. 2015, The ParaView Guide: A Parallel Visualization Application (Clifton Park, NY, USA: Kitware, Inc.)

Bagenal, F., & Dols, V. 2020, Journal of Geophysical Research: Space Physics, 125, e2019JA027485, doi: https://doi.org/10.1029/2019JA027485

Dall'Osso, S., Israel, G. L., & Stella, L. 2006, A&A, 447, 785, doi: 10.1051/0004-6361:20052843

De Colle, F., Lin, D. N. C., Chen, C., & Li, G. 2025, Monthly Notices of the Royal Astronomical Society, 539, 3459, doi: 10.1093/mnras/staf707

Dedner, A., Kemm, F., Kröner, D., et al. 2002, Journal of Computational Physics, 175, 645,

doi: https://doi.org/10.1006/jcph.2001.6961

Drell, S. D., Foley, H. M., & Ruderman, M. A. 1965, PhRvL, 14, 171, doi: 10.1103/PhysRevLett.14.171

Goldreich, P., & Lynden-Bell, D. 1969, ApJ, 156, 59, doi: 10.1086/149947

Hansen, B. M. S., & Lyutikov, M. 2001, Monthly Notices of the Royal Astronomical Society, 322, 695, doi: 10.1046/j.1365-8711.2001.04103.x

Harris, C. R., Millman, K. J., van der Walt, S. J., et al. 2020, Nature, 585, 357, doi: 10.1038/s41586-020-2649-2

Harten, A., Lax, P. D., & Leer, B. v. 1983, SIAM Review, 25, 35, doi: 10.1137/1025002

Hunter, J. D. 2007, Computing in Science & Engineering, 9, 90, doi: 10.1109/MCSE.2007.55

Lai, D. 2012, ApJL, 757, L3,

doi: 10.1088/2041-8205/757/1/L3

Laine, R. O., & Lin, D. N. C. 2011, ApJ, 745, 2, doi: 10.1088/0004-637X/745/1/2

Lanza, A. F. 2013, A&A, 557, A31, doi: 10.1051/0004-6361/201321790

Laune, J., Li, R., & Lai, D. 2024, ApJ, 975, 296, doi: 10.3847/1538-4357/ad7117 Lee, E. J., & Owen, J. E. 2025, Carving the Edges of the Rocky Planet Population.

https://arxiv.org/abs/2501.17241

Li, J., Ferrario, L., & Wickramasinghe, D. 1998, The Astrophysical Journal, 503, L151, doi: 10.1086/311546

Mahlmann, J. F., & Beloborodov, A. M. 2025, The Astrophysical Journal Letters, 981, L17, doi: 10.3847/2041-8213/adb5fd

Mignone, A., Bodo, G., Massaglia, S., et al. 2007, ApJS, 170, 228, doi: 10.1086/513316

Mignone, A., & Tzeferacos, P. 2010, Journal of Computational Physics, 229, 2117, doi: https://doi.org/10.1016/j.jcp.2009.11.026

Mignone, A., Tzeferacos, P., & Bodo, G. 2010, Journal of Computational Physics, 229, 5896, doi: https://doi.org/10.1016/j.jcp.2010.04.013

Miyoshi, T., & Kusano, K. 2005, Journal of Computational Physics, 208, 315,

doi: https://doi.org/10.1016/j.jcp.2005.02.017

Most, E. R., & Philippov, A. A. 2022, MNRAS, 515, 2710, doi: 10.1093/mnras/stac1909

—. 2023, ApJL, 956, L33, doi: 10.3847/2041-8213/acfdae
Neubauer, F. 1990, Advances in Space Research, 10, 25, doi: https://doi.org/10.1016/0273-1177(90)90083-C

Neubauer, F. M. 1980, Journal of Geophysical Research: Space Physics, 85, 1171,

doi: https://doi.org/10.1029/JA085iA03p01171

—. 1998, Journal of Geophysical Research: Planets, 103, 19843, doi: https://doi.org/10.1029/97JE03370

Piddington, J. H. 1967

Piro, A. L. 2012, ApJ, 755, 80, doi: 10.1088/0004-637X/755/1/80

Preusse, S., Kopp, A., Büchner, J., & Motschmann, U. 2006, A&A, 460, 317, doi: 10.1051/0004-6361:20065353

Ressler, S. M., Combi, L., Li, X., Ripperda, B., & Yang, H. 2024, ApJ, 967, 70, doi: 10.3847/1538-4357/ad3ae2

- Roe, P. 1981, Journal of Computational Physics, 43, 357, doi: https://doi.org/10.1016/0021-9991(81)90128-5
- Saur, J. 2018, Electromagnetic Coupling in Star-Planet Systems, ed. H. J. Deeg & J. A. Belmonte (Cham: Springer International Publishing), 1877–1893, doi: 10.1007/978-3-319-55333-7_27
- Stokes, G. G. 1851, Transactions of the Cambridge Philosophical Society, 9, 8
- Strugarek, A. 2023, in Star-planet interactions, ed.
 L. Bigot, J. Bouvier, Y. Lebreton, A. Chiavassa, &
 A. Lèbre (Les Ulis, France: EDP sciences), 1–21
- Strugarek, A., Brun, A. S., Matt, S. P., & Réville, V. 2014, ApJ, 795, 86, doi: 10.1088/0004-637X/795/1/86
- —. 2015, ApJ, 815, 111, doi: 10.1088/0004-637X/815/2/111

- Tiwari, S. S., Pal, E., Bale, S., et al. 2020, Powder Technology, 365, 115,doi: https://doi.org/10.1016/j.powtec.2019.01.037
- Wang, J.-S., Yang, Y.-P., Wu, X.-F., Dai, Z.-G., & Wang,
- Wang, J.-S., Yang, Y.-P., Wu, A.-F., Dai, Z.-G., & Wang, F.-Y. 2016, The Astrophysical Journal Letters, 822, L7, doi: 10.3847/2041-8205/822/1/L7
- Wu, K., Cropper, M., Ramsay, G., & Sekiguchi, K. 2002, Monthly Notices of the Royal Astronomical Society, 331, 221, doi: 10.1046/j.1365-8711.2002.05190.x
- Yamaleev, N. K., & Carpenter, M. H. 2009, Journal of Computational Physics, 228, 4248, doi: https://doi.org/10.1016/j.jcp.2009.03.002